Chemical Science

EDGE ARTICLE

Check for updates

All publication charges for this article have been paid for by the Royal Society of Chemistry

Elucidating the reversed proton relay mechanism: dual regulatory role of pendant carboxylates relevant to water oxidation

Taolue Liu,[a] Yu Wei,[a] Guojie Gao,[a] Mingxia Guo,[a] Jinxuan Liu, [iD] [a] Xin Ding, [iD] *[c] Yingying Li [iD] *[b] and Yan Gao [iD] *[a]

To elucidate the "reversed proton relay" mechanism in mediating water oxidation under neutral conditions, we designed two Ru(II) complexes: $[Ru^{II}(tda-\kappa-N^3O)(isoq)_2]$ (**Ru1**), featuring a coordination-oversaturated pendant carboxylate, and $[Ru^{II}(tpc-\kappa-N^3O)(isoq)_2][PF_6]$ (**Ru1'**), lacking this structural motif. In **Ru1**, coordination oversaturation renders the carboxylate dynamically accessible, enabling it to function as a proton switch that extracts protons from the metal center. Density functional theory (DFT) calculations, along with comparative experimental data, confirm that the carboxylate facilitates catalytic switching: in its deprotonated state, it stabilizes key intermediates and promotes O_2 evolution *via* reversed proton transfer. Online high-resolution mass spectrometry (HRMS) further identifies key intermediates, providing direct experimental evidence for this unconventional proton relay pathway. Collectively, these findings uncover a previously unrecognized mode of proton transfer and offer valuable mechanistic insights for the rational design of efficient water oxidation catalysts under neutral conditions.

Introduction

The increasing global demand for sustainable energy has made the development of new energy storage forms a crucial research topic, with the conversion of solar energy into chemical energy being a central focus of sustainable energy projects.[1–3] Solar fuel conversions produce a wide variety of products, from simple molecules like hydrogen (H_2) and ammonia (NH_3) to complex substances such as hydrocarbons, alcohols, and acids.[4–7] The design of such conversion processes—particularly those for producing chemical fuels using solar energy—often draws inspiration from the principles of natural photosynthesis, with the core mechanism being the $4e^-/4H^+$ water oxidation half-reaction driven by Photosystem II (PSII): this reaction efficiently facilitates energy transfer and electron transfer processes, providing a key energy foundation for subsequent carbon fixation. In nature, this reaction is catalyzed by the Mn_4CaO_5 cluster in PSII, with an overpotential of approximately 160 mV and a reaction rate of 100–400 s^{-1}.[8–11] However, its catalytic performance deteriorates significantly when removed from the natural environment, highlighting the urgent need for efficient artificial photosynthetic catalysts.

The proton-electron coupled transfer mechanism observed in natural photosynthesis offers valuable guidance for the design of artificial catalysts. In the hydrogen evolution reaction (HER), the "proton relay" effect improves hydrogen production efficiency by regulating the local proton concentration near the metal center. Functional groups such as amino and carboxylic acids facilitate proton delivery, thereby promoting H–H bond formation.[12–17] In the case of the oxygen evolution reaction (OER), pendant groups are often introduced to enhance catalytic performance. However, most studies have focused on empirical correlations between pendant group structures and catalytic activity, while overlooking the fact that these modifications represent a proton relay mechanism in reverse: a directional shift from proton donation (as in HER) to proton extraction, tailored to meet the kinetic requirements of water oxidation.[18–27] This oversight highlights a fundamental design dilemma in early research: excessive reliance on saturated coordination environments to stabilize the metal center, while improving catalyst stability, can impede the approach of H_2O to the metal site. On the other hand, it also affects the rate of directional transfer of protons (H^+) from the metal center to the solvent, which is a key factor limiting the efficiency of many catalytic systems. The metal center's coordination environment regulates proton-transfer capability (by providing open sites or hindering migration), thereby determining catalytic efficiency (Scheme 1a). For example, pendant ligands create additional proton migration channels ($L^{Eq}M + H_2O \rightarrow L^{Eq}(OH)-MH \rightarrow L^{Eq}(OH)-M + H^+$; $L^{Eq}(OH)-M \rightarrow L^{Eq}(O)-MH \rightarrow L^{Eq}(O)-M + H^+$; L^{Eq} = equatorial ligand), similar to their role in H_2-splitting

[a] *Dalian University of Technology, State Key Laboratory of Fine Chemicals, Dalian 116024, China. E-mail: dr.gaoyan@dlut.edu.cn*

[b] *Zhengzhou Normal University, School of Chemistry and Chemical Engineering, Zhengzhou 450044, China. E-mail: liyingying@zznu.edu.cn*

[c] *Qingdao University, College of Chemistry and Chemical Engineering, Qingdao 266071, China. E-mail: dingxin@qdu.edu.cn*
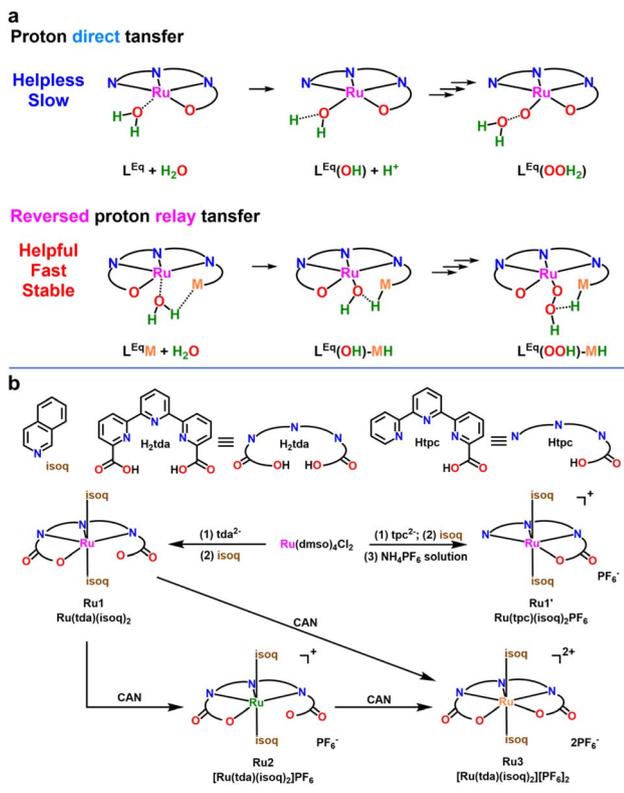
Scheme 1 (a) Direct proton transfer in the absence of reversed proton relay and efficient proton transfer *via* reversed proton relay mechanism.[a] (b) Synthetic routes of complexes. [a]Schematic illustration. Actual conditions may vary. Axial ligands are omitted for clarity.

$(L^{Eq}M + H_2 \rightarrow L^{Eq}(H)-MH)$, where both pathways optimize the transport efficiency of reaction intermediates by modulating the coordination environment.

Herein, we propose a "reversed proton relay" mechanism, wherein modulation of ligand field electron density enables efficient proton abstraction without disrupting a fully coordinated metal center. To verify this, two Ru(II) complexes were designed: Ru(tda)(isoq)$_2$ (**Ru1**), with a pendant carboxylate group formed *via* coordination oversaturation, and Ru(tpc)(isoq)$_2$PF$_6$ (**Ru1′**), with saturated coordination (Scheme 1b). Experimental and computational results showed that the carboxylate in **Ru1** functions as a bifunctional switch, facilitating proton transfer and modulating catalytic activity. Under neutral/alkaline conditions, this group mediates reversed proton transfer through hydrogen-bonded water networks, establishing an optimal reaction microenvironment to drive Ru oxidation state evolution. This process enables efficient water oxidation with significantly enhanced catalytic performance compared to the saturated-coordination **Ru1′**. More critically, online intermediate capture experiments (Fig. 4) visually elucidate the directional proton transfer pathway from the carboxylate group to the Ru center. This experimental visualization not only directly validates the theoretical predictions of the "reversed proton relay" mechanism but also provides a foundational basis for understanding the catalytic performance data. This study revises the traditional catalyst design that

excessively pursues saturated coordination, and establishes a new design strategy for neutral water oxidation catalysts through the "reversed proton relay" mechanism of over-saturated coordination.

Experimental

Materials

All solvents were purified and dried by standard methods prior to use. Commercial reagents (Shanghai Aladdin) were used without further purification, except for trimethylsilyl cyanide (Anhui Energy Chemical). All organometallic reactions were performed using a Schlenk line under strictly oxygen-free conditions, with a continuous argon flow maintained throughout the process and a gas outlet sealed by a glycerol trap to prevent air ingress. Key reagents including Ru(dmso)$_4$Cl$_2$, 2,2′:6′,2″-terpyridine-6,6″-dicarboxylic acid (**H$_2$tda**), and 2,2′:6′,2″-terpyridine-6-carboxylic acid (**Htpc**), were synthesized and purified according to literature procedures.[18,28–30] High-purity deionized water was prepared *via* Milli-Q nanopure filtration. ^{1}H-NMR and ^{13}C-NMR spectra were acquired on Bruker Avance II 400 or III 500 spectrometers. MS analysis was performed at Dalian University of Technology using a Micromass Q-TOF Micro and Bruker MALDI-TOF spectrometer. More details are available in the SI.

Preparation of catalysts

[Ru^{II}(tda-κ-N^{3}O)(isoq)$_2$], Ru1. Ru(dmso)$_4$Cl$_2$ (76 mg, 0.156 mmol; 1 equiv.), **H$_2$tda** (47 mg, 0.146 mmol) and Et$_3$N (0.15 mL) were suspended in anhydrous MeOH (5 mL) and degassed. The mixture was degassed, refluxed for 6 h, and then cooled to room temperature. The resulting brown precipitate was collected by filtration, washed with MeOH and ether, and dried. The solid was redispersed in water (4 mL), and an EtOH solution of isoquinoline (404 mg/3 mL) was added. The mixture was refluxed overnight. The mixture was refluxed overnight, concentrated *in vacuo*, and the residue was dissolved in MeOH. The product was precipitated by adding ether, collected by filtration washed with petroleum ether, and dried. The reaction operations were carried out under an argon atmosphere. The final product was obtained as a red solid (82 mg, 0.12 mmol, 82.7% yield). ^{1}H-NMR (500 MHz, CD$_3$OD) δ: 9.35 (s, 2H), 8.67 (d, $J = 8.0$ Hz, 2H), 8.47 (dd, $J = 8.0$ Hz, $J = 1.5$ Hz, 2H), 8.12 (t, $J = 8.0$ Hz, 1H), 7.97 (dd, $J = 7.5$ Hz, $J = 1.5$ Hz, 3H), 7.94 (m, $J = 7.5$ Hz, 3H), 7.74 (d, 8.0 Hz, 2H), 7.69 (td, $J = 7.5$ Hz, $J = 1.0$ Hz, 2H), 7.63 (d, 6.5 Hz, 2H), 7.60 (dd, $J = 7.0$ Hz, $J = 1.0$ Hz, 2H), 7.42 (d, 7.0 Hz, 2H). ^{13}C-NMR (125 MHz, CD$_3$OD) δ: 172.89, 163.68, 159.56, 158.85, 143.60, 137.91, 136.09, 133.78, 133.36, 129.80, 129.60, 128.77, 127.86, 127.25, 125.21, 125.14, 123.03. UV-vis [λ$_{max}$, nm (ε, M^{-1} cm^{-1})]: 280 (40 727), 326 (37 455), 377 (15 727) and 530 (5591).

[Ru^{II}(tpc-κ-N^{3}O)(isoq)$_2$][PF$_6$], Ru1′. Ru(dmso)$_4$Cl$_2$ (88 mg, 0.18 mmol, 1 equiv.), **Htpc** (50 mg, 0.18 mmol), and Et$_3$N (0.15 mL) were suspended in anhydrous EtOH (5 mL) and degassed. The mixture was degassed, refluxed for 6 h, and then cooled to room temperature. The resulting brown precipitate was

collected by filtration, washed with EtOH and ether, and dried. The solid was redispersed in an EtOH solution of isoquinoline (233 mg/7 mL). After refluxing overnight, the brown-red solution was concentrated *in vacuo*. The residue was dissolved in minimal EtOH, precipitated with excess NH_4PF_6/H_2O, and collected by filtration. The solid was washed with cold water, dried, and purified by column chromatography (CH_2Cl_2/MeOH: 30/1) to afford the product. The final product was obtained as a red solid (81 mg, 0.10 mmol, 57.7% yield). ^{1}H-NMR (500 MHz, CD_3OD) δ: 9.80 (sd, $J = 5.0$ Hz, 1H), 8.83 (d, $J = 8.5$ Hz, 1H), 8.77 (d, $J = 8.5$ Hz, 1H), 8.71 (s, 1H), 8.55 (d, $J = 8.5$ Hz, 1H), 8.34 (d, $J = 7.5$ Hz, 1H), 8.15 (t, $J = 8.0$ Hz, 1H), 8.04 (m, 3H), 7.84 (m, 7H), 7.74 (t, $J = 7.0$ Hz, 2H), 7.64 (t, $J = 8.0$ Hz, 2H), 7.57 (d, $J = 6.5$ Hz, 2H). ^{13}C-NMR (150 MHz, CD_3OD) δ: 173.27, 161.44, 160.48, 158.49, 158.12, 155.05, 153.36, 152.95, 147.62, 141.94, 138.88, 136.13, 134.85, 132.96, 132.30, 130.52, 129.90, 128.65, 126.90, 126.05, 125.72, 124.82, 124.36, 123.24, 122.10. UV-vis [λ_{max}, nm (ε, M^{-1} cm^{-1})]: 273 (41 136), 311 (36 182), 381 (15 818).

Characterization and analysis methods

Mass spectrometry (MS) analyses were conducted using electrospray ionization (ESI) on three instruments: a Micromass UK Limited Q-TOF Micro, a Thermo Scientific LTQ Orbitrap XL, and a Bruker MALDI-TOF spectrometer. UV-vis absorption spectra were recorded on a Shimadzu UV-1900 spectrophotometer (Japan) with 1 cm quartz cuvettes. NMR spectra were acquired using Bruker Avance II 400 or Avance III 500 spectrometers. Solution pH values were measured by a calibrated Shanghai Leici PHS-3C pH meter, using standard solutions at pH 4.00, 6.86, and 9.18 for calibration prior to analysis. More details are available in the SI.

Single crystals of **Ru1** and **Ru1′** were obtained by dissolving the complexes in ethanol-based solvent systems (with trifluoroethanol or water), placing the solutions in sealed flasks containing diethyl ether for vapor diffusion crystallization, and isolating dark red crystals after slow evaporation. Crystal structures were determined by mounting the crystals on a Bruker D8 Venture single-crystal diffractometer, collecting diffraction data with Cu or Mo target, solving the structures using Olex2, and refining with SHELXL.[31]

Electrochemical experiments were performed on a CHI 630E workstation (Shanghai Chenhua) using a three-electrode system. Glassy carbon disk electrodes ($\Phi = 2$ mm) served as the working electrode, platinum wires ($\Phi = 1$ mm) as the counter electrode, and pH-dependent reference electrodes were employed: Hg/Hg_2SO_4 (saturated K_2SO_4) for acidic, Ag/AgCl (saturated KCl) for neutral, Hg/HgO (0.1 M KOH) for basic conditions, and all referenced to NHE. Reference electrodes were calibrated with $Ru(bpy)_3^{2+}$ ($Ru^{III}/Ru^{II} = 1.26$ V *vs.* NHE). Cyclic voltammetry (CV), differential pulse voltammetry (DPV), and coulometry were applied to analyze redox behaviors across pH ranges.

The oxygen evolution was monitored by a NEOFOX-KIT-PATCH oxygen sensor kit (Ocean Optics, USA), and the catalytic water oxidation reaction was driven by ceric ammonium nitrate (CAN, Ce^{IV}) as the oxidant.

Mass spectrometry measurements to capture water oxidation intermediates were performed using Q-TOF, LTQ Orbitrap XL, and MALDI-TOF spectrometers. The reaction solution, prepared by dissolving the catalyst in water containing 27% CF_3CH_2OH (1.1 mM), was mixed with a certain amount of Ce^{IV} aqueous solution under stirring. After thorough mixing, the reaction solution was immediately transferred to a HRMS for analysis. The pH meter indicated that the pH of the reaction is 5.7 approximately after mixing with 4 eq Ce^{IV}.

DFT calculations

DFT calculations were performed with the Gaussian 16 program to elucidate the mechanism of the Ru-catalyzed water oxidation.[32] All calculations were carried out using the B3LYP-D3 functional.[33,34] The 6-31G(d,p) basis set was employed for non-metal atoms, and the Stuttgart-Dresden effective core potential (SDD) was used for the Ru atom.[35] Analytical frequency calculations were performed at the same level as the geometry optimization to verify the local minima nature of various stationary points (no imaginary frequency) and saddle-point property of the transition state (only one imaginary frequency). The final energies were from single-point calculations employing the SMD implicit solvation model.[36] All non-metal elements were depicted by 6–311 + G(2df,2p). The value of -6.3 kcal mol^{-1} of solvation energy of water in aqueous solution from the experiment was used.[37] All species were corrected with a concentration-dependent energy term (1.9 kcal mol^{-1}), with an additional 4.3 kcal mol^{-1} adjustment specifically for water. Protonation states were determined *via* pK_a calculations for all plausible intermediates. The solvation energy of a proton was taken from the experiment (-264.0 kcal mol^{-1}). Redox potentials were referenced to the standard hydrogen electrode (SHE, 4.281 V).

Results and discussion

Catalyst synthesis and structural characterization

We designed two catalysts—[Ru^{II}(tda-κ-N^3O)(isoq)$_2$] (**Ru1**) and [Ru^{II}(tpc-κ-N^3O)(isoq)$_2$] (**Ru1′**)—to systematically investigate the dual role of the reversed relay group (Scheme 1b): (1) as a molecular switch regulating catalytic activity, and (2) as a dynamic reversed proton relay modulating the catalytic microenvironment.[38,39] The ligands **H₂tda** and **Htpc** were synthesized from 2,2′:6′,2″-terpyridine (trpy) *via* three steps (Fig. S1–S6).[28–30] Ru(dmso)$_4$Cl$_2$ first reacted with **H₂tda**, followed by isoquinoline (isoq), to yield the red-wine complex **Ru1** in 82.7% yield. **Ru1'** was synthesized similarly in 52.7% yield (Fig. S7–S14). X-ray crystallography confirmed both of complexes are low-spin d^6 Ru(II) distorted octahedral structure (Fig. 1a, b, S15, S16, and Table S1).[20,22,40]

This structural feature of **Ru1** shows consistency with the previously reported Ru(tda)(py)$_2$ catalyst in terms of crystal structure: the carbon skeletons of the tda^{2-} ligands in the equatorial planes of both catalysts exhibit similar bond angles and bond lengths.[18] However, notable differences are observed in the ligand – related carboxylate groups (COO^-). The C–O
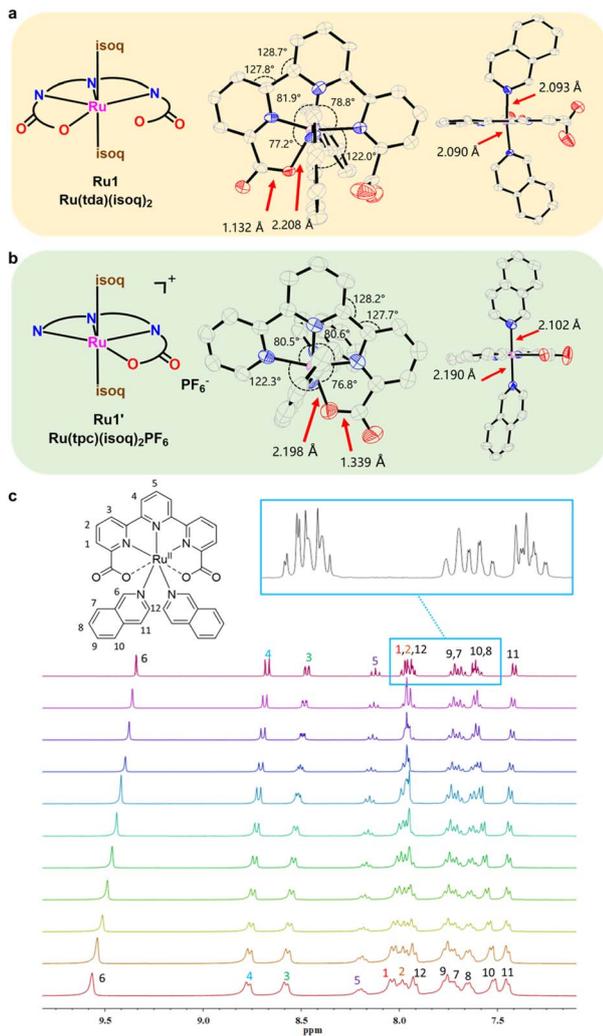
Fig. 1 (a) X-ray ORTEP plots of [Ru^{II}(tda-κ-N^{3}O)(isoq)$_2$], Ru1. (b) X-ray ORTEP plots of [Ru^{II}(tpc-κ-N^{3}O)(isoq)$_2$]$^+$, Ru1'. Ellipsoids are plotted at 50% probability. Color codes: Ru, purple; N, blue; O, red; C, gray. H are not shown. (c) Variable temperature ^{1}H-NMR spectra of Ru(tda)(isoq)$_2$ in CD$_3$OD.

bond length of the carboxylate group shortens from 1.284 Å in the pyridine-containing system to 1.132 Å in the isoquinoline-containing system, accompanied by an elongation of the Ru–O bond length at the metal center (from 2.198 Å (py) to 2.208 Å (isoq)). In the axial direction, the introduction of isoq leads to a significant increase in the Ru–N bond length (from 2.083 Å (py) to 2.093 Å (isoq)). This phenomenon suggests that when the axial ligand is switched from pyridine to isoquinoline, the resulting electronic effects may alter the state of the relay ligand of the catalyst in the solution microenvironment. Subsequent proton-coupled electron transfer (PCET) steps in the Pourbaix diagram and relative energies for Ru1 species in SI have repeatedly demonstrated that the relay ligand undergoes protonation in acidic solutions.

Furthermore, the intrinsic fast low-barrier dynamic exchange process of the pendant relay ligand in Ru1 enables it to stably function as a molecular switch. Specifically, the crystal

structure of Ru1 reveals a significantly asymmetric feature: the O–Ru bond length is only 2.208 Å, while the adjacent non-coordinated O atom is 3.689 Å away from the Ru center (Fig. 1a and b). For an asymmetric complex like Ru1', such structural disparities would typically manifest as asymmetric peak distributions in the ^{1}H-NMR spectrum. However, Ru1 exhibits highly symmetric characteristic peaks in ^{1}H-NMR. This proves that it is a highly stable, "resonance-like" structure. Variable temperature ^{1}H-NMR experiments on Ru1 (198 K, CD$_3$OD, Fig. 1c) further confirm its structural stability. Even at low temperatures, this complex maintains highly symmetric ^{1}H-NMR features without any resonance peak splitting caused by slowed proton transfer kinetics in the side chains. For example, the overlapping hydrogen signals (7.5–8.0 ppm) at room temperature resolve into well-defined peaks upon cooling: the 7.95 ppm multiplet is assigned to hydrogens on the tda^{2-} ligand (C$_1$/C$_2$) and the isoquinoline (C$_{12}$), while the 7.70 ppm and 7.60 ppm multiplets dissociate into triplets and doublets at low temperatures, corresponding to hydrogens on the isoquinoline (C$_9$/C$_7$ and C$_8$/C$_{10}$), respectively. These findings conclusively establish that the two COO–Ru groups on the transverse ligands of Ru1 in solution maintain identical chemical states due to a rapid dynamic exchange process with an extremely low energy barrier, which is the fundamental mechanism underlying the observed symmetric ^{1}H NMR spectrum.[20,22] While this dynamic behavior inhibits stable water coordination in solution, it preserves robust metal-ligand integrity and ensures reversible switching essential for catalytic modulation.

In contrast, Ru1' lacks this pendant group entirely. This key structural difference dictates their catalytic behavior: the free carboxylate in Ru1 forms hydrogen bonds with water, stabilizing protons and enhancing oxygen evolution. This structural difference underpins the distinct catalytic mechanisms of reversed proton relay: Ru1 can modulate Ru-Aqua species formation by regulating the carboxylate's electron density. Specifically, the deactivation of reversed proton relay (protonating COO$^-$) not only disrupts hydrogen-bond network formation but also disables the mechanism entirely. This precise control over proton transfer pathways highlights the unique advantage when other pathways must compete with water oxidation. The ability to toggle the carboxylate's protonation state thus provides a powerful tool for optimizing catalytic efficiency in complex reaction environments.

Reversed proton relay effects control active species generation

A spectrophotometric redox titration experiment was designed to investigate the effect of protonation on the ligand's electronic density in the catalyst. Protonation of the carboxylate group was hypothesized to reduce Ru-Aqua formation (i.e., "switching off" the catalytic activity) and experimentally validated. During the redox titration under acidic conditions, incremental additions of the corresponding oxidant equivalents were performed, and UV-vis spectral changes were monitored (Fig. 2a and b). The stabilized solution spectra show strong alignment with the Ru2/Ru3 reference spectra independently prepared by introducing an equivalent CAN in Ru1 ethanol solution and isolating the
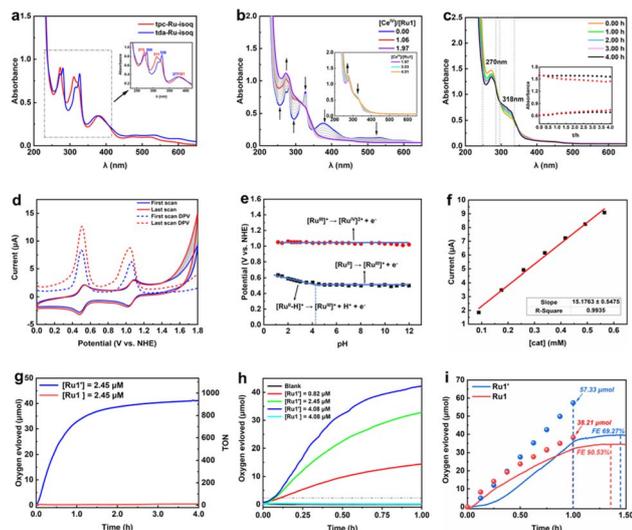
Fig. 2 (a) UV-vis spectra of complexes Ru1 (blue), Ru1′ (red). (b) UV-vis spectra of Ru1 (22 μM) (blue) in 0.1 M triflic acid, and successive additions of 0.152 equiv. of Ce^{IV} (1 mM) (grey) up to 2 equiv. Inset: to 4 equiv. (c) Stability test of Ru3, (37.5 μM) in pH 7. Inset: plot of absorbance vs. time for $\lambda = 270$ and 318 nm at pH 1.0 (black) and pH 7.0 (red). (d) RCV ($v = 30$ mV s^{-1}) of 1.1 mM of Ru1 in pH 7 (27% CF$_3$-CH$_2$OH). (e) Pourbaix diagram for the Ru species derived from Ru1. The detailed species states are simplified and represented solely by the oxidation state of Ru, the charge number, and the ligand status. (f) Plot of the i_{cat} – [cat] at 1.80 V in pH 7 (27% CF$_3$CH$_2$OH). (g) Comparison of long-term oxygen production capabilities for Ru1 and Ru1′. (h) Oxygen evolution curve at various concentrations of Ru1′. (i) Oxygen evolution curve of electrolysis (background-free). Inset point: theoretical O$_2$ value calculated from the total charge quantity at this time.

products via saturated KPF$_6$ precipitation (Scheme 1b and Fig. S17). Absorption peaks at 250–350 nm were attributed to π–π* transitions of the catalyst ligands, while the weaker visible-region absorption were identified as metal-to-ligand charge transfer (MLCT), Ru-d → bda-π*. Notably, under one catalytic cycle, no spectral evidence of oxidation states higher than Ru^{IV} (Ru3) was observed. At a Ce(IV) equivalent of 1.06, absorption peaks at 377 nm and 530 nm disappeared, with low absorbance remaining stable in subsequent titrations. The absorbance at 326 nm slowly decreased with modest change, while a sharp 270 nm peak appeared. Compared to UV-vis spectra of Ru3, when 2 eq. of CAN was added, the 326 nm oxidation absorption of Ru2 was not clearly distinguishable, likely due to insufficient oxidation time. This variation exhibits a significant difference compared to the previously reported Ru(tda)(py)$_2$ system: after the Ru^{II} → Ru^{IV} oxidation occurs, Ru^{IV}(isoq) does not show a prominent peak-valley at 318 nm as observed in Ru^{IV}(py), but instead presents an observable concave feature. As the titration progressed, the 270 nm absorbance increased while absorbance beyond 300 nm decreased and stabilized. After adding oxidants for one catalytic cycle, the catalyst solution's UV-vis characteristics were monitored for 50 minutes and remained stable, showing no decay toward Ru2 and Ru3 trends. Under neutral conditions, Ru3 solution (Ru^{IV}) exhibited significant attenuation, which is attributed to the catalyst's redox potential exceeding the theoretical water oxidation potential leading to

a disproportionation reaction in this chemical environment (Fig. 2c). However, its dissolution rate is slower than that of Ru^{IV}(tda)(py)$_2$ catalyst, indicating that the introduction of the isoquinoline ligand modifies the aqueous microenvironment, thereby slowing the attack rate of water molecules on the relay-type catalyst and consequently delaying the formation of the Ru-Aqua active species during water oxidation.[18] This characteristic effectively accounts for the absence of distinct new peaks attributable to the Ru-Aqua active species in subsequent repetitive cyclic voltammetry (RCV) scans (Fig. 2d), but concurrently enhancing the feasibility of online detection for reaction intermediates at various stages.

Reversed proton relay effects improve electrochemical performance

Redox titration indicates that Ru3 (oxidized from Ru1) undergoes neutral disproportionation in the absence of external oxidation, yet this does not imply a loss of catalytic activity. When the driving force is sufficient (RCV and electrolysis), Ru1 exhibits both greater stability and higher activity compared to Ru1′ (Fig. 2d and S20). Compared to Ru1 with an additional reverse proton transfer group, Ru1′ lacking this group exhibits catalytic center deactivation during cyclic water oxidation, accompanied by substantial electron loss. These findings confirm that the introduction of a pendant reversed proton relay enhances the stability of the catalyst during usage and extends its lifespan. Similarly, the stabilizing effect on the catalytic microenvironment through such characteristics has been reported in studies of analogous catalysts.[20,22,41,42] CVs at different scan rates reveals that the surface redox processes of the Ru1 and Ru1' electrodes are diffusion-controlled according to the Randles–Sevcik equation (Fig. S18 and S19). The shift of Ru1 redox peak in CV from stable 0.51 V under neutral and alkaline conditions to 0.60 V under acidic conditions is because the carboxyl reversed proton transfer group on the equatorial ligand in the 0.1 M triflic acid solution undergoes protonation as previously discussed. The increase in current between 1.4 and 1.7 V in high pH is attributed to the catalytic oxidation of water by the active Ru-Aqua species produced by carboxylate reversed proton transport. Obviously, electrochemical tests confirm Ru1 exhibits higher OER performance in neutral conditions (Fig. S20) than Ru1′ (no regulation) or in acidic conditions (suppressed carboxylate). After repetitive cyclic voltammetry (RCV), Ru1 showed a significant increase in catalytic current under neutral Na$_2$SO$_4$ conditions, while the currents in acid solutions decreased (Fig. 2d). Combined with DPV and spectrophotometric redox titration results, these potential transitions are associated with the redox processes of Ru^{II} → Ru^{III} + e$^-$ and Ru^{III} → Ru^{IV} + e$^-$. The Pourbaix diagram analysis also confirms that the redox behavior of Ru1 is pH-independent across most pH ranges (Fig. 2e). Notably, when the pH decreases, the single-electron transfer process (Ru^{III}/Ru^{II}) transitions to a distinctly different PCET process (Ru^{II}–H → Ru^{III} + H$^+$ + e$^-$). The pH-independent Ru^{III}/Ru^{IV} step in Ru1 (Ru(tda)(isoq)$_2$) exhibits a significantly lowered potential, decreasing from 1.10 V (Ru(tda)(py)$_2$) to 1.04 V vs. NHE. This

indicates that the **Ru1** exhibits enhanced reducibility in its Ru^{IV} state. However, this characteristic renders the key reaction pathway, which relies on Ru^{IV} undergoing nucleophilic attack to form the Ru^{IV}–OH active species, thermodynamically unfavorable. This disadvantage consequently impedes the formation of active Ru-hydrate species. Specifically, under neutral conditions, the decay rate of the corresponding UV characteristic peak during the oxygen evolution process *via* high-valent disproportionation in $Ru(tda)(py)_2$ is significantly faster than that in the corresponding process of $Ru(tda)(isoq)_2$.[18] Based on the DFT calculation data regarding the relative energies for **Ru1** species from the SI, the protonation process of this catalyst exhibits a low energy barrier under acidic conditions (Fig. S31). Specifically, the pK_a value of 6.14 for Ru^{II}–H effectively substantiates that isoquinoline (isoq) as an axial ligand induces a spatial effect distinctly different from that of pyridine. This spatial effect difference further modulates the microenvironment of the equatorial active site, thereby facilitating the formation of optimized PCET steps within the pH range of 1–4. **Ru1** is highly stable in acidic aqueous solutions, making the formation of hydrated **Ru-Aqua** species difficult. On the other hand, **Ru1′** without COO^- shows greater stability in acidic environments, consistent with the preferences of the vast majority of catalysts. Consecutive detection of various oxidation states of Ru^{II}, such as $Ru^{II} \rightarrow Ru^{III}$ and Ru^{II}–$H_2O \rightarrow Ru^{IV}$=O, was also observed in different pH (Fig. S21).[43]

Electrochemical analysis also confirms the oxygen evolution for two catalysts originated from a water nucleophilic attack (WNA): the i_{cat} of 1.8 V (NHE) in different pH linearly related to [cat] of two complexes and independent of scan rate (Fig. 2f, S22–S24 and Table S2).[44] The corresponding experimental conditions and electrochemical methods are also suppled in SI. **Ru1** exhibits higher TOF (0.0263 s^{-1}) under acidic conditions than **Ru1′** (0.0092 s^{-1}) in electrochemical evaluations. Given the activation energy demand associated with the relay-type proton relay mechanism, this characteristic makes it essential to provide activation time for the catalysts and conduct synchronous online oxygen evolution monitoring. The macroscopic water oxidation performance evaluation results obtained in this way have more reliable reference value compared with the electrochemical activity data calculated from a single cyclic voltammetry test.

Reversed proton relay enables superior oxygen evolution

Electrochemical studies and spectroscopic evidence show that the reversed proton relay (the COO^-) can enhance catalytic activity and stability under neutral conditions by optimizing the metal microenvironment during water oxidation. To validate this capacity of facilitating PCET through intermediate stabilization *via* hydrogen bonding, real time O_2 concentration monitoring was performed in neutral *via* electrolysis tests. **Ru1** achieved 18.16 μmol oxygen within the first 30 minutes, delivering an oxygen production 1.5 times that of **Ru1′** (12.27 μmol), thereby confirming the critical role of the reversed proton relay mechanism in neutral water oxidation. On the other hand, as expected, the carboxyl group's protonation under acidic

conditions disables its reversed proton transfer capacity, resulting in negligible oxygen evolution of **Ru1** over 4 hours in triflic acid. In contrast, **Ru1′**, which exhibited favorable performance in acid solution tests, demonstrated a linear relationship between oxygen evolution rate and catalyst concentration, eventually reaching saturation over time. These macroscopic oxygen evolution experiments corroborate that the carboxylate molecular switch significantly enhances water oxidation reaction activity in low $[H^+]$ concentration.

A four-hour study using cerium ammonium nitrate (Ce(IV)) as the oxidant in acidic homogeneous aqueous solutions and calculating the Turnover Number (TON, n_{O2}/n_{cat}) was conducted. **Ru1′** achieved a TON of 934.3 after four hours, while **Ru1** showed negligible activity (TON = 10.4, Fig. 2g). This stark contrast highlights the strong pH-dependence of reversed proton relay. Under strong acid conditions, despite Ce(IV)'s high oxidative capability, **Ru1** fails to drive the water oxidation reaction effectively. The oxygen production level of **Ru1** remains around the origin regardless of the catalyst content. In contrast, **Ru1′** exhibits a strong response with oxygen production rates far outperforming **Ru1**. The linear relationship between oxygen production rate and catalyst concentration yields a high TOF = 0.39 s^{-1} for **Ru1′**, confirming its superior catalytic performance in acidic conditions (Fig. 2h, S25 and S26). The poor catalytic activity of reversed proton relay catalyat **Ru1** in acidic solutions due to failure to form effective **Ru-Aqua** intermediates, while **Ru1′** is highly active in acidic solutions. In contrast, the catalytic behavior reverses in neutral 0.1 M sodium sulfate solutions. When electrolyzing the catalysts on composite electrodes (CP) at 1.7 V *vs.* NHE for one hour, **Ru1′** initially shows a higher current, but after subtracting the oxygen evolution from the blank carbon paper, **Ru1** produces more oxygen overall in the initial stage (Fig. 2i, S27A and B). After 1.5 hours, **Ru1** reaches 34.6 μmol oxygen, while **Ru1′** peaks at 39.7 μmol. But **Ru1** achieves a Faradaic efficiency of 90.53%, compared to 69.27% for **Ru1′**. This once again demonstrates the catalytic behavior of "reversed proton relay" varies with pH inseparably (Fig. 3a). Notably, **Ru1′**'s stability under neutral conditions was further investigated by immersing a used composite electrode in CF_3-CH_2OH for two weeks. UV-vis spectra confirmed the formation of divalent **Ru1**, indicating its stable state after catalysis termination is Ru^{II} state (Fig. S27C and D).

Calculation of catalytic pathways and capture of intermediates

The properties and experimental results indicate that that the reversed proton relay operate through distinct mechanistic pathways depending on pH conditions. Further research from the perspective of energy using online experiments and computational modeling is needed to fully understand its mechanisms when reversed proton relay activated. DFT calculations reveal that **Ru1** follows a WNA mechanism, where electron loss occurs on the peroxide's outer oxygen while Ru remains in the Ru^{III} state (in Fig. 3b).[32–37] It plays a crucial role uncovering the catalytic mechanism of **Ru1** with free carboxylate group during water oxidation. Online high-resolution
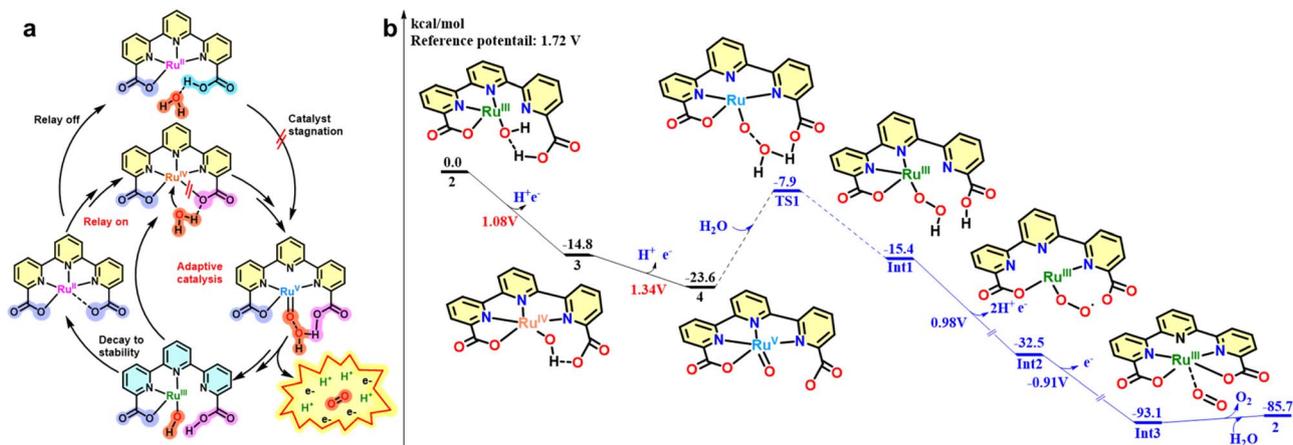
Fig. 3 (a) The water oxidation catalytic pathway of reversed proton relays. (b) Gibbs energy diagram of water oxidation catalyzed by **2**. Axial ligands are omitted for clarity.

mass spectrometry (HRMS) validates mechanism by detecting key intermediates in different oxidation states.

Although water coordination to **Ru1** forming Ru^{II}–OH$_2$ (**1**) is endergonic ($\Delta G = +8.7$ kcal mol^{-1}, Fig. S28), the active cycle initiates from the Ru^{III}–OH$_2$ (**2**) state, not low-valent Ru^{II}. The UV-vis spectra collected after the oxygen evolution electrolysis experiment confirmed that the Ru^{II} state merely represents the stabilized form of the catalyst in its inactive state. For Ru^{III}–OH$_2$ (**2**), a proton transfers to the carboxylate group with a single electron oxidation, with a calculated redox potential of 0.24 V. A

PCET process ($E^o = 1.08$ V) from **2** forms Ru^{IV}–OH (**3**, Ru–O$_1 = 1.85$ Å) through a thermodynamically favorable process ($\Delta G = -14.8$ kcal mol^{-1}), which then forms Ru$^V = $O (**4**) through another PCET step ($E^o = 1.34$ V; $\Delta G = -8.8$ kcal mol^{-1}) in Fig. S29. Ru$^V = $O triggers O–O bond formation via nucleophilic water attack at a transition state **TS1** (Ru–O$_1 = 1.72$ Å, O$_1$–O$_2$ distance $= 2.28$ Å, $\Delta G^* = 15.7$ kcal mol^{-1}) that collapses into hydroperoxide **Int1** (Ru^{III}–OOH) and superoxide **Int2** (Ru^{III}–OO$^\bullet$) intermediates before final O$_2$ release (Fig. S30). Then closing the catalytic cycle and involving the combination of the second water
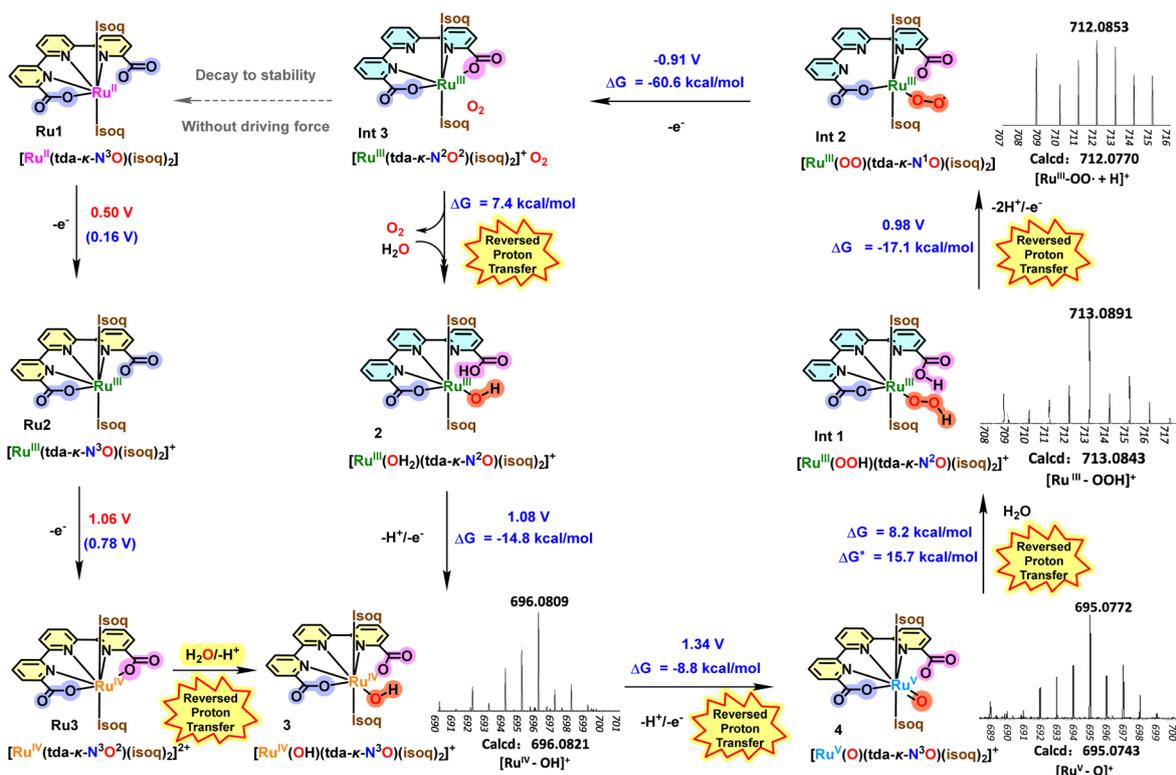

Fig. 4 "Reversed Proton Relay" catalytic pathway and intermediate capture. The red potential comes from experiments and the blue potential comes from calculations.

with the Ru center to form $Ru^{III}-OH_2$ (**2**). Compared to **Ru-Aqua**, the direct oxidation of **Ru1** to **Ru2** has a potential of 0.16 V, the calculated redox potential from **Ru2** to **Ru3** is only 0.78 V (Fig. S31). Previous experiments indicate that **Ru1** oxidation to **Ru3** serves as a prerequisite step for generating the active **Ru-Aqua** species prior to catalytic cycle initiation. Thus, catalytic pathway of reversed proton relay **Ru1** involves single-electron oxidation of **Ru1** to **Ru3**, water attack to form **3**, and entry into the **Ru-Aqua** O_2 evolution cycle, solely cycling between $Ru^{III/IV/V}$-Aqua states. Real-time mass spectrometry reveals sequential intermediates of **Ru1** in water oxidation (Fig. 4), validating DFT predictions. Initially, **Ru1** $[Ru^{II} + Na]^+$ appears at $m/z = 702.32$ (Q-TOF, calcd. 702.0691). After the first Ce(IV) addition, **Ru2** $[Ru^{III}]^+$ emerges ($m/z = 679.33$ [Q-TOF], 679.0796 [LTQ XL], calcd. 679.0803), confirmed as $Ru^{III}PF_6$ ($m/z = 824.0434$, MALDI, calcd. 824.0417). A second Ce(IV) equivalent produces $[Ru^{IV}]^{2+}$ ($m/z = 339.5412$, LTQ, calcd. 339.5931). Under reduced acidity, four Ce(IV) additions yield $[Ru^{IV}-OH]^+$ ($m/z = 696.0809$, LTQ, calcd. 696.0821) via hydroxide attack. And PCET forms $[Ru^V = O]^+$ ($m/z = 695.0772$, LTQ, calcd. 695.0743) a high-valence ruthenium intermediate with a seven-coordination geometry. Water attack on $[Ru^V = O]^+$ generates **Int1** $[Ru^{III}-OOH]^+$ ($m/z = 713.0891$, LTQ, calcd. 713.0843), which evolves into **Int2** $[Ru^{III}-OO^{\bullet} + H]^+$ ($m/z = 712.0853$, LTQ, calcd. 712.0770) through proton loss. Final oxidation forms transient **Int3**, completing the cycle via O=O bond cleavage.

HRMS/MS data confirm all intermediates, elucidating the actively regulatory pathway of reversed proton relay mechanism (COO^- as experimental example) in water oxidation. The experimental verification of key intermediates not only validates the DFT theoretical model, but also deepens the understanding of the proton transfer dynamic process during the activation of such molecular catalytic switches. Moreover, intermediates data and the theoretical calculation of pK_a for each intermediate from DFT are presented (Fig. S32–S36 and Scheme S1). Furthermore, this study, referencing the research findings of the Ahlquist group, analyzed the feasibility of the "the carboxyl peroxide mechanism" for the catalyst with a microenvironment influenced by spatial effects when the isoquinoline substitutes the pyridine ligand, from an energetic perspective in SI.[42,45] The alternative pathway **TS1′** involving direct coupling of the oxyl radical with the carboxylate oxygen atom exhibits a low activation barrier of 2.1 kcal mol^{-1} (Fig. S37). This situation may arise when acid radical salts act as transport groups for reverse proton relay oxygen production. However, this pathway is thermodynamically unfavorable due to the subsequent challenges in C–O bond cleavage and O_2 release, and is therefore rejected.

Conclusions

In summary, **Ru1** and **Ru1′**, with carboxylate mediated group as the variable, were designed to validate the "reversed proton relay" mechanism, the core driver of neutral water oxidation. These complexes systematically elucidated the dual role of pendant carboxylate groups, formed via coordination oversaturation, as both a molecular switch and a reversed proton relay in water oxidation catalysis. The tda^{2-} ligand framework forms a six-coordinate Ru(II) complex with a dynamic coordination site, enabling the carboxylate to toggle between protonated, catalytically inhibitory states under acidic conditions and deprotonated, proton-transfer-facilitating states under neutral to alkaline conditions. HRMS and DFT analyses confirmed that this dual regulation optimizes proton transfer and catalytic activity, effectively resolving the trade-off between coordination saturation and dynamic proton transport. This work establishes a new design paradigm that integrates molecular switching and proton relay functionalities for neutral water oxidation catalysts.

Author contributions

Y. Gao conceived the idea for this study and designed the research. T. Liu conducted the research. Y. Li and X. Ding helped with the analysis and interpretation of the data. T. Liu wrote the manuscript and all authors assisted with editing, analysis, and interpretation.

Conflicts of interest

The authors declare no competing financial interest.

Data availability

The data supporting this article have been included as part of the supplementary information (SI). Supplementary information: experimental procedures; compounds synthesis and characterization (NMR, HRMS, and crystal data); electrochemical data. See DOI: https://doi.org/10.1039/d5sc07030a.

CCDC 2250881 and 2383557 contain the supplementary crystallographic data for this paper.[46a,b]

Acknowledgements

Notes and references

1 N. S. Lewis, *Science*, 2016, **351**, aad1920.
2 J. Gong, C. Li and M. R. Wasielewski, *Chem. Soc. Rev.*, 2019, **48**, 1862–1864.
3 P. Chen, Y. Xiao, S. Li, X. Jia, D. Luo, W. Zhang, H. J. Snaith, Q. Gong and R. Zhu, *Chem. Rev.*, 2024, **124**, 10623–10700.
4 R. M. Evans, B. Siritanaratkul, C. F. Megarity, K. Pandey, T. F. Esterle, S. Badiani and F. A. Armstrong, *Chem. Soc. Rev.*, 2019, **48**, 2039–2052.
5 D. He, G. Huang, J. Hu, J. Ding, W. Liu, L. Chen, W. Yan, J. Zhu, S. Zhu, Q. Chen, X. Jiao and Y. Xie, *Adv. Energy Mater.*, 2024, **15**, 2402889.
6 A. Agosti, Y. Nakibli, L. Amirav and G. Bergamini, *Nano Energy*, 2020, **70**, 104510.
7 S. Li, Y. Zhou, X. Fu, J. B. Pedersen, M. Saccoccio, S. Z. Andersen, K. Enemark-Rasmussen, P. J. Kempen,

C. D. Damsgaard, A. Xu, R. Sažinas, J. B. V. Mygind, N. H. Deissler, J. Kibsgaard, P. C. K. Vesborg, J. K. Nørskov and I. Chorkendorff, *Nature*, 2024, **629**, 92–97.

8 N. Vereshchuk, M. Gil-Sepulcre, A. Ghaderian, J. Holub, C. Gimbert-Suriñach and A. Llobet, *Chem. Soc. Rev.*, 2023, **52**, 196–211.

9 Y. Umena, K. Kawakami, J.-R. Shen and N. Kamiya, *Nat.*, 2011, **473**, 55–60.

10 N. Cox, D. A. Pantazis, F. Neese and W. Lubitz, *Acc. Chem. Res.*, 2013, **46**, 1588–1596.

11 B. Zhang and L. Sun, *Chem. Soc. Rev.*, 2019, **48**, 2216–2264.

12 D. Dolui, S. Khandelwal, A. Shaik, D. Gaat, V. Thiruvenkatam and A. Dutta, *ACS Catal.*, 2019, **9**, 10115–10125.

13 S. N. Chowdhury, S. Biswas, P. Das, S. Paul and A. N. Biswas, *Inorg. Chem.*, 2020, **59**, 14012–14022.

14 S. Lin, S. Banerjee, M. T. Fortunato, C. Xue, J. Huang, A. Y. Sokolov and C. Turro, *J. Am. Chem. Soc.*, 2022, **144**, 20267–20277.

15 Y. Qiu, D. Ray, L. Yan, X. Li, M. Song, M. H. Engelhard, J. Sun, M.-S. Lee, X. Zhang, M.-T. Nguyen, V.-A. Glezakou, Y. Wang, R. Rousseau and Y. Shao, *J. Am. Chem. Soc.*, 2023, **145**, 26016–26027.

16 F. Droghetti, F. Begato, M. Raulin, G. Musiu, G. Licini, M. Natali and C. Zonta, *Angew. Chem., Int. Ed.*, 2024, **63**, e202408316.

17 M. Haake, B. Reuillard, M. Chavarot-Kerlidou, C. Costentin and V. Artero, *Angew. Chem., Int. Ed.*, 2024, **63**, e202413910.

18 R. Matheu, M. Z. Ertem, J. Benet-Buchholz, E. Coronado, V. S. Batista, X. Sala and A. Llobet, *J. Am. Chem. Soc.*, 2015, **137**, 10786–10795.

19 R. Matheu, M. Z. Ertem, C. Gimbert-Suriñach, J. Benet-Buchholz, X. Sala and A. Llobet, *ACS Catal.*, 2017, **7**, 6525–6532.

20 N. Vereshchuk, R. Matheu, J. Benet-Buchholz, M. Pipelier, J. Lebreton, D. Dubreuil, A. Tessier, C. Gimbert-Suriñach, M. Z. Ertem and A. Llobet, *J. Am. Chem. Soc.*, 2020, **142**, 5068–5077.

21 N. Vereshchuk, J. Holub, M. Gil-Sepulcre, J. Benet-Buchholz and A. Llobet, *ACS Catal.*, 2021, **11**, 5240–5247.

22 T. Liu, S. Zhan, N. Shen, L. Wang, Z. Szabó, H. Yang, M. S. G. Ahlquist and L. Sun, *J. Am. Chem. Soc.*, 2023, **145**, 11818–11828.

23 S. Bhunia, A. Rana, S. Hematian, K. D. Karlin and A. Dey, *Inorg. Chem.*, 2021, **60**, 13876–13887.

24 Q. Huo, J. Cao, L. Mi, J. Shao, M. Lv, X. Chen, H. Yang, X. Chai, Q. Hu and C. He, *J. Mater. Chem. A*, 2023, **11**, 1335–1342.

25 N. Wang, X.-P. Zhang, J. Han, H. Lei, Q. Zhang, H. Zhang, W. Zhang, U.-P. Apfel and R. Cao, *Chin. J. Catal.*, 2023, **45**, 88–94.

26 M. Li, T. Zhang, Y. Shi, C. He and C. Duan, *Angew. Chem., Int. Ed.*, 2024, **63**, e202406161.

27 D. Chen, W. Li, J. Liu and L. Sun, *Energy Environ. Sci.*, 2025, **18**, 3120–3128.

28 V.-M. Mukkala, C. Sund, M. Kwiatkowski, P. Pasanen, M. Högberg, J. Kankare and H. Takalo, *Helv. Chim. Acta*, 1992, **75**, 1621–1632.

29 C. Galaup, J.-M. Couchet, S. Bedel, P. Tisnès and C. Picard, *J. Org. Chem.*, 2005, **70**, 2274–2284.

30 I. P. Evans, A. Spencer and G. Wilkinson, *J. Chem. Soc., Dalton Trans.*, 1973, 204–209.

31 O. V. Dolomanov, L. J. Bourhis, R. J. Gildea, J. A. K. Howard and H. Puschmann, *J. Appl. Crystallogr.*, 2009, **42**, 339–341.

32 M. J. Frisch, G. W. Trucks, H. B. Schlegel, G. E. Scuseria, M. A. Robb, J. R. Cheeseman, G. Scalmani, V. Barone, G. A. Petersson, H. Nakatsuji, X. Li, M. Caricato, A. V. Marenich, J. Bloino, B. G. Janesko, R. Gomperts, B. Mennucci, H. P. Hratchian, J. V. Ortiz, A. F. Izmaylov, J. L. Sonnenberg, D. Williams-Young, F. Ding, F. Lipparini, F. Egidi, J. Goings, B. Peng, A. Petrone, T. Henderson, D. Ranasinghe, V. G. Zakrzewski, J. Gao, N. Rega, G. Zheng, W. Liang, M. Hada, M. Ehara, K. Toyota, R. Fukuda, J. Hasegawa, M. Ishida, T. Nakajima, Y. Honda, O. Kitao, H. Nakai, T. Vreven, K. Throssell, J. A. Jr, J. E. Peralta, F. Ogliaro, M. J. Bearpark, J. J. Heyd, E. N. Brothers, K. N. Kudin, V. N. Staroverov, T. A. Keith, R. Kobayashi, J. Normand, K. Raghavachari, A. P. Rendell, J. C. Burant, S. S. Iyengar, J. Tomasi, M. Cossi, J. M. Millam, M. Klene, C. Adamo, R. Cammi, J. W. Ochterski, R. L. Martin, K. Morokuma, O. Farkas, J. B. Foresman and D. J. Fox, *Gaussian 16 Revision A.03.*, Gaussian, Inc., Wallingford CT, 2016.

33 A. D. Becke, *J. Chem. Phys.*, 1993, **98**, 5648–5652.

34 S. Grimme, J. Antony, S. Ehrlich and H. Krieg, *J. Chem. Phys.*, 2010, **132**, 154104.

35 D. Andrae, U. HaiuBermann, M. Dolg, H. Stoll and H. PreuB, *Theor. Chim. Acta*, 1990, **77**, 123–141.

36 A. V. Marenich, C. J. Cramer and D. G. Truhlar, *J. Phys. Chem. B*, 2009, **113**, 6378–6396.

37 D. M. Camaioni and C. A. Schwerdtfeger, *J. Phys. Chem. A*, 2005, **109**, 10795–10797.

38 T. Liu, CSD Commun., 2024, Deposited Date: 22 March 2023.

39 T. Liu, CSD Commun., 2024, Deposited Date: 12 September 2024.

40 L. Duan, F. Bozoglian, S. Mandal, B. Stewart, T. Privalov, A. Llobet and L. Sun, *Nat. Chem.*, 2012, **4**, 418–423.

41 R. Matheu, M. Z. Ertem, M. Pipelier, J. Lebreton, D. Dubreuil, J. Benet-Buchholz, X. Sala, A. Tessier and A. Llobet, *ACS Catal.*, 2018, **8**, 2039–2048.

42 S. Zhan, J. A. De Gracia Triviño and M. S. G. Ahlquist, *J. Am. Chem. Soc.*, 2019, **141**, 10247–10252.

43 T. Fan, L. Duan, P. Huang, H. Chen, Q. Daniel, M. S. G. Ahlquist and L. Sun, *ACS Catal.*, 2017, **7**, 2956–2966.

44 M. Okamura, M. Kondo, R. Kuga, Y. Kurashige, T. Yanai, S. Hayami, V. K. K. Praneeth, M. Yoshida, K. Yoneda, S. Kawata and S. Masaoka, *Nature*, 2016, **530**, 465–468.

45 A. Kundu, S. K. Barman and S. Mandal, *Inorg. Chem.*, 2022, **61**, 1426–1437.

46 (*a*) CCDC 2250881: Experimental Crystal Structure Determination, 2025, DOI: **10.5517/ccdc.csd.cc2fk72b**; (*b*) CCDC 2383557: Experimental Crystal Structure Determination, 2025, DOI: **10.5517/ccdc.csd.cc2l08yv**.